ADVANCED ENERGY MATERIALS

www.advenergymat.de

Surface Doping to Enhance Structural Integrity and Performance of Li-Rich Layered Oxide

Shuai Liu, Zepeng Liu, Xi Shen, Weihan Li, Yurui Gao, Mohammad Norouzi Banis, Minsi Li, Kai Chen, Liang Zhu, Richeng Yu, Zhaoxiang Wang, Xueliang Sun, Gang Lu, Qingyu Kong, Xuedong Bai, and Liquan Chen*

The Li-rich layer-structured oxides are regarded as one of the most promising cathode materials for their high energy density but suffer from severe problems such as capacity fading, poor rate performance, and continuous potential dropping. These issues are addressed here by surface doping of niobium (Nb) and other heavy ions in a Li-rich Mn-based layered oxide, $Li_{1.2}Mn_{0.54}Ni_{0.13}Co_{0.13}O_2$. The doped ions are verified to be located in the Li-layer near the oxide surface; they bind the slabs via the strong Nb—O bonds and "inactivate" the surface oxygen, enhancing the structural stability. The specific capacity of the modified oxide reaches 320 mAh g^{-1} in the initial cycle, 94.5% of which remains after 100 cycles. More importantly, the average discharge potential drops only by 136 mV in this process. The findings of this study illustrate the importance of inactivating the surface oxygen in suppressing the cation mixing in the bulk, providing an effective strategy for designing high-performance Li-rich cathode materials.

1. Introduction

High energy density is of primary importance for battery applications in consumer electronics and electric vehicles. The Li-rich layered oxides[1] are regarded as the most promising cathode materials for the next-generation Li-ion batteries (LIBs) for their high energy density and low cost.[2] However, these materials suffer from crucial drawbacks such as capacity fading, continuous potential dropping, etc.,[3] due mostly to continuous migration of the transition metals (TMs) into the Li layer and the resultant gradual structural degradation from layered to spinel or rocksalt.

Surface modification including coating, etching and passivating the electrode surface[2,4] have been proved effective in controlling the capacity decline of the Li-rich oxides by suppressing the surface corrosion and electrolyte decomposition. However, it fails to work in preventing the discharge potential dropping. In addition, the lattice mismatch between the active host and the coating guest results in splitting of the coating layer during long-term cycling. Cation and anion doping have been proposed to improve the cycling performance of the Li-rich oxides by impeding the TM migration,[5] but cannot stop the discharge potential dropping either.

The TM migration is known to start on the surface upon deep delithiation and propagate into the bulk of the Li-rich oxides.[6] Numerous studies have demonstrated the correlation between loss of the surface oxygen and TM migration.[7] It was reported that generation of oxygen vacancies facilitates the TM migration and surface structural transformation.[8] Theoretical calculations[9] and experimental studies[10] in our group pointed out that the severe distortion of the MnO_6 octahedron due to generation of oxygen and/or Li vacancies and variation of the Mn—O bond

Dr. S. Liu, Dr. Z. Liu, Prof. Z. Wang, Prof. L. Chen
Key Laboratory for Renewable Energy
Chinese Academy of Sciences
Beijing Key Laboratory for New Energy Materials and Devices
Institute of Physics
Chinese Academy of Sciences
Beijing 100190, China
E-mail: zxwang@iphy.ac.cn

Dr. S. Liu, Dr. Z. Liu, Dr. L. Zhu, Prof. R. Yu, Prof. Z. Wang, Prof. L. Chen
School of Physical Sciences
University of Chinese Academy of Sciences
Beijing 100190, China

Dr. X. Shen, Prof. R. Yu
Laboratory for Advanced Materials and Electron Microscopy
Institute of Physics
Chinese Academy of Sciences
Beijing 100190, China

Dr. W. Li, Dr. M. N. Banis, Dr. M. Li, Prof. X. Sun
Department of Mechanical and Materials Engineering
University of Western Ontario
London, Ontario N6A 5B9, Canada

Dr. Y. Gao, Prof. G. Lu
Department of Physics and Astronomy
California State University Northridge
Northridge, CA 91330–8268, USA

Dr. K. Chen, Dr. Q. Kong
Synchrotron Soleil
L'Orme des Merisiers St-Aubin, 91192 Gif-sur-Yvette, France

Dr. L. Zhu, Prof. X. Bai
State Key Laboratory for Surface Physics
Institute of Physics
Chinese Academy of Sciences
Beijing 100190, China

DOI: 10.1002/aenm.201802105

length during delithiation are the fundamental driving force for the Mn migration in Li_2MnO_3. Therefore, anchoring or inactivating the surface oxygen is critical in immobilizing the TM ions and in stabilizing the structure and performances of the material.

Our density functional theory (DFT) calculations[9a] indicate that, of the eight elements (Ti, V, Cr, Fe, Co, Ni, Zr, and Nb) studied, Nb is the best substituent for Mn in Li_2MnO_3 because it binds O more strongly than Mn does and its substitution suppresses the O evolution upon Li removal. In addition, the ionic radius of Nb^{5+} is comparable to that of Mn^{4+} and Li^+, making it feasible for the Nb^{5+} ions to enter the Li or TM layers.[11] Similar are the case for the Ti^{4+} and Zr^{4+} ions.

Herein we chose Nb^{5+}, Ti^{4+}, and Zr^{4+} ions for surface doping in one of the most popular Li-rich layered oxides, $Li_{1.2}Mn_{0.54}Ni_{0.13}Co_{0.13}O_2$ (or $0.5Li_2MnO_3 \cdot 0.5LiNi_{1/3}Co_{1/3}Mn_{1/3}O_2$, LMR hereafter). The guest ions enter the surface by a depth of four to five atomic layers and occupy the Li layer. They bind the TM—O slabs of the LMR and inactivate its surface oxygen by the strong Nb—O bonds. With these, the layered-to-spinel transformation is suppressed and the structural reversibility is enhanced, stabilizing the discharge potential and other performances.

2. Results and Discussion

2.1. Surface Structure of LMR-Nb

High-angle annular dark-field (HAADF) imaging is sensitive to the heavy atoms (Ni, Co, Mn, etc.) since its contrast is proportional to $Z^{1.7}$ (Z for the atomic number) in the aberration-corrected scanning transmission electron microscopy (STEM).[12] **Figure 1**a illustrates a well-defined layered structure ($R\bar{3}m$ space group) for the as-prepared LMR-Nb, clean of any TM ions in the Li layer in the bulk. In addition, Rietveld refinement of the X-ray diffraction (XRD) patterns of LMR and LMR-Nb indicates that the surface doping does not change the lattice parameters (Tables S3 and S4, Supporting Information). However, heavy ions appear in the Li layer near the surface (Figure 1b), in strong contrast with the homogeneously well-ordered light and heavy atoms throughout the as-prepared LMR (Figure S1, Supporting Information). The strong peaks in the line-scan intensity profile (inset of Figure 1b) reveal that the heavy ions enter the surface by about five atomic layers (≈1.5 nm).

The arrangement of the light atoms such as Li and O can be better detected by annular bright-field (ABF) imaging as its contrast is proportional to $Z^{1/3}$.[12] Figure 1c demonstrates that the light atoms near the surface in LMR-Nb are similarly arranged as those in LMR (Figure S1, Supporting Information), indicating that Nb-doping does not induce any detectable lattice mismatch in LMR-Nb.

Atomic-resolution energy-dispersive X-ray spectroscopy mapping gives an overview of the distribution of the dominating Mn and the doped Nb ions near the surface (Figure 1d). The Mn atoms are found distributed homogeneously throughout the particle while the Nb atoms assemble near the surface, matching well with the surface doping layer in Figure 1e. These observations clearly demonstrate that the doped Nb ions enter the lattice of the LMR subsurface.

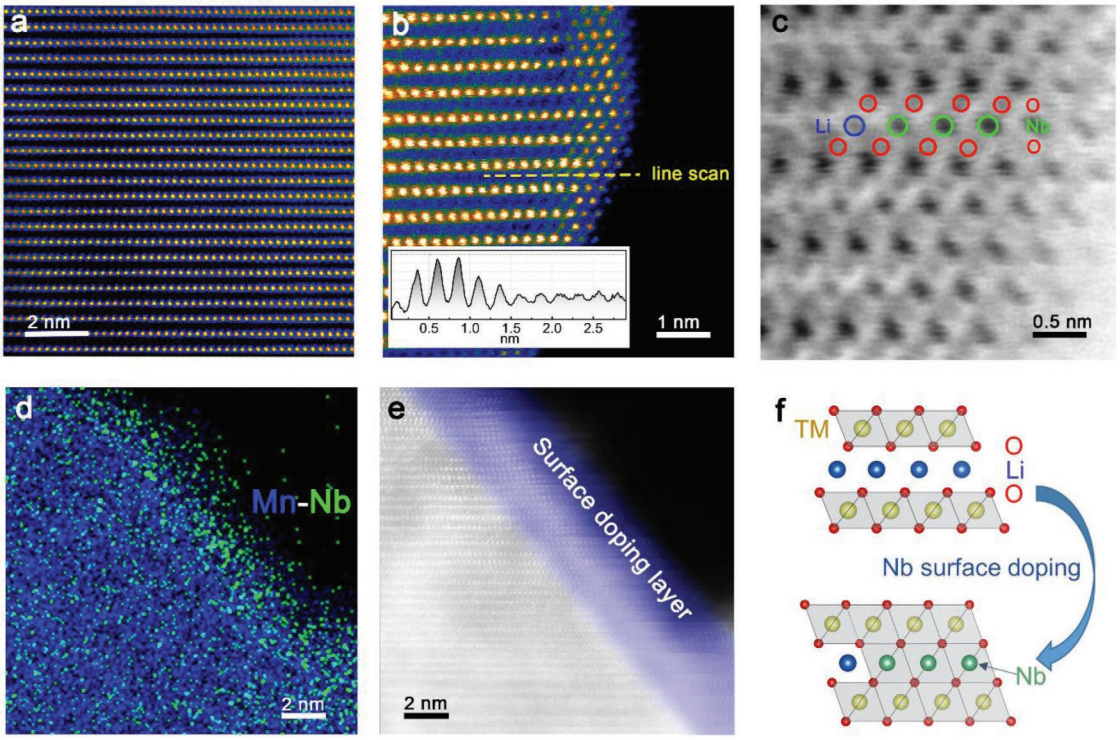

Figure 1. The STEM images of the LMR-Nb sample. a) the HAADF image in the bulk; b) the HAADF image near the surface; c) the ABF enlarged image of the surface area in (b); d) the EDS mapping of Mn and Nb for the corresponding HAADF image of e) the surface doping layer; f) the schematic process of surface doping and the Nb-enhanced surface structure.

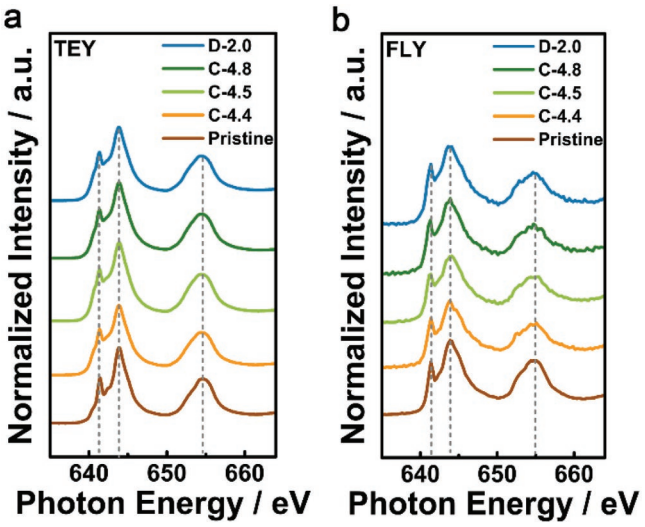

Figure 2. The Mn $L_{2,3}$ edge SXAS spectra of the LMR-Nb in the a) the TEY and b) the FLY modes at various charge/discharge states in the first cycle.

DFT calculations further suggest that the doped Nb ions prefer to enter the Li layer (Figure S2, Supporting Information) though direct experimental recognition of the Nb occupancy is currently not available. With Li_2MnO_3 (C2/m) as the model host structure, the formation energy of Nb substitution for Li in the Li layer, for Li in the TM layer, and for TM in the TM layer is calculated to be −2.87, 0.66, and −2.06 eV, respectively, if the substitution occurs in the bulk. However, the energy sharply decreases to −5.09 eV for Nb in the Li layer and −4.87 eV for Nb in the TM layer, respectively, if the substitution is within the three outermost surface layers of Li_2MnO_3. In addition, the formation energy of Nb substitution for Li in the Li layer is 3.53 eV lower than for substitution for Li in the TM layer near the surface. These reveal that the doped Nb ions prefer to stay in the Li layer rather than the TM layer and that Nb instead of TM is more likely to be found in the Li layer near the surface. Therefore, the heavy atoms detected in the Li layer are believed to be Nb in Figure 1. More details for the calculations methods and results can be found in the DFT section and Tables S1 and S2 in the Supporting Information.

Figure 1f schematically compares the surface structure of LMR and LMR-Nb. Clearly, substitution of Nb^{5+} for Li^+ in the Li layer will enhance the integrity of the surface structure of LMR since the strong Nb—O bonding binds the O—TM—O slabs or the TMO_6 octahedrons near the surface into a whole.

2.2. Charge Compensation in LMR-Nb

It was reported[13] that the Mn^{4+} ion is reduced upon the initial discharge of LMR and participates in the charge compensation in the subsequent cycles. Changing of the Mn oxidation state affects the configuration of the octahedral oxygen and promotes the TM migration.[8a] In addition, disproportional reaction of the Mn^{3+} ions results in dissolution of the Mn^{2+} ions, especially at elevated temperatures.

Soft X-ray adsorption structural (SXAS) spectroscopy was performed to find out the electronic structure and local environment of the metal and oxygen ions at various charge/discharge states (Figure S3, Supporting Information). The detection depth by the total electron yield (TEY) mode is a few nanometers while that by the fluorescence yield (FLY) mode is up to hundred nanometers.[14] Two peaks appear at ≈643.8 and ≈654.5 eV, respectively in the Mn $L_{2,3}$ edge spectrum of fresh LMR (Figure S4, Supporting Information), indicating that its Mn ions exist as Mn^{4+}. Surface doping does not change the Mn $L_{2,3}$ edge spectrum (Figure S4, Supporting Information) and charge/discharge processing cannot affect the Mn $L_{2,3}$ edge spectrum of LMR-Nb (**Figure 2**). The Mn^{4+} ions remain inert in the bulk and on the surface of LMR-Nb. Keeping the Mn^{4+} ions inactive is beneficial for avoiding distortion of the TMO_6 octahedron and stabilizing the LMR-Nb structure. The slight distortion of the FLY spectrum is attributed to the self-absorption of the Mn^{4+} ions.[15]

No recognizable differences are observed in the Nb L_3 edge spectrum in the bulk or on the surface of LMR-Nb (Figure S5, Supporting Information). In addition, the Nb ion remains Nb^{5+} during the first cycle, indicating that the Nb ion is inert in LMR-Nb throughout the initial cycling.

Figure 3a compares the O *K* edge of the as-prepared LMR-Nb and LMR. The two pre-edge (below 535 eV) peaks are for the transition of the O_{1s} electrons to the hybridized TM_{3d} and O_{2p} orbitals.[16] The FLY O *K* edge of LMR-Nb is almost the same as that of LMR, indicating that surface doping does not affect the bulk oxygen of the material. Integration of the intensity of the pre-edge peaks (Figure S6, Supporting Information) indicates that Nb doping reduces the TM_{3d}-O_{2p} hybridization on the LMR-Nb surface,[16] suppressing the O oxidation and TM migration near the surface. In addition, the weak 533.8 eV peak for the oxygen in the residual Li_2CO_3[17] on LMR disappears after Nb doping, implying that the LMR-Nb surface is more stable than the LMR surface against the air, probably due to the reduced Li content on the former.

Figure 3b shows the FLY O *K* edge of LMR-Nb at various states. When the cell is charged to 4.4 V, the pre-edge peak shifts to a lower energy. This shifting can be better recognized in the differential spectrum (Figure S7a, Supporting Information) and is attributed to the TM (only Ni and Co in this work; Figure S8, Supporting Information) oxidation.[13d,18] As the material is charged from 4.4 to 4.8 V, a new peak appears at 530.8 eV (marked with red dash line in Figure 3b and Figure S7a in the Supporting Information). Gent et al.[13d,19] reported this peak in the FLY O *K* edge of $Li_{1.17}Ni_{0.21}Co_{0.08}Mn_{0.54}O_2$ charged to ≈4.5 V and attributed it to the signature of the oxygen redox. On the basis of a series of advanced characterization, they verified that the O redox is a bulk phenomenon. This peak grows with increasing charge potential and disappears as the cell is discharged to 2.0 V. These reveal the reversible charge compensation of the bulk oxygen.

The broad band around 540 eV, known as the shape resonance peak due to its intrinsic sensitivity to the bond length,[13c,20] is for the transition of the O_{1s} electron to the hybridized O_{2p} and TM_{4sp} orbitals,[15] or the transition of the O_{1s} electron to the antibonding σ^* state.[13c,16] It shifts blue during charging and restores to its original position as the material is discharged to 2.0 V (Figure 3b), suggesting the decrease and increase of the TM—O bond length, respectively.

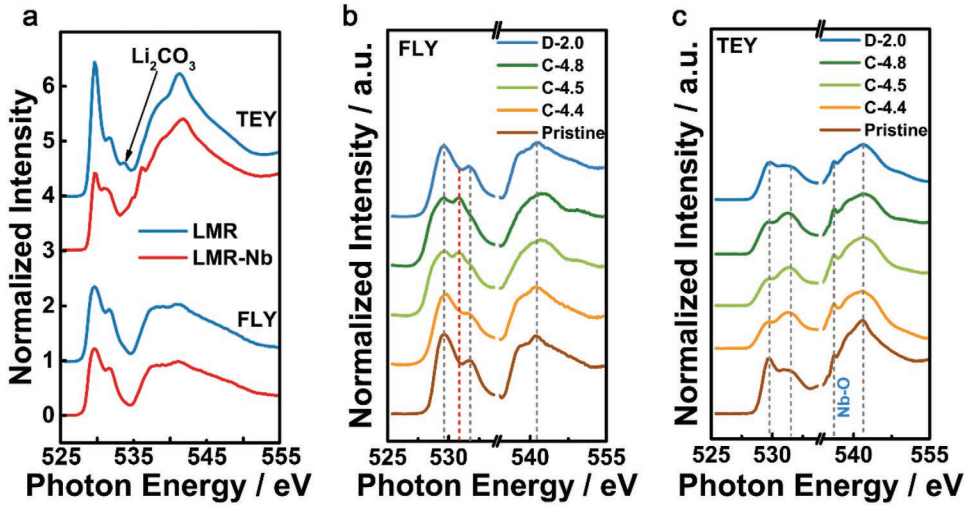

Figure 3. a) The O *K* edge SXAS spectra of the LMR and LMR-Nb powder in the TEY and FLY modes, the O *K* edge spectrum of the LMR-Nb in the b) FLY and c) TEY modes at various charge/discharge states in the first cycle.

In comparison with the reversible redox of oxygen in the bulk, the activation of the surface oxygen is significantly suppressed as no oxygen redox peak appears in the TEY O *K* edge (Figure 3c). In addition, no shifting was observed for the bond-length sensitive band above 4.4 V, indicating the stabilized TM—O bond length near the surface. The strong Nb—O bond ensures the robust O ligand framework, prevents the O oxidation (inactivates the surface oxygen), and weakens the hybridization on the surface. The weak peak at 536.1 eV in Figure 3c is assigned to the O *K* edge of the Nb—O bond (Figure S9, Supporting Information).

The intensity of the pre-edge peaks is determined with two factors, the number of the holes (unoccupied states) in the TM_{3d} and O_{2p} orbitals and the TM_{3d}-O_{2p} hybridization.[16] The intensity is expected to increase since the number of the holes increases due to Co/Ni oxidation during charging. However, their intensities decline in the TEY mode. This implies that the TM_{3d}-O_{2p} hybridization becomes reduced, probably due to the presence of the tough Nb—O ionic bond and the resultant constant length of the TM—O bond on the surface, before the material is charged to 4.4 V. On one hand, the strong Nb—O bond pins the e_g-O_{2p} hybridization. On the other hand, the decrease of the radius of the oxidized Co/Ni ions leads to shrinkage of the TM_{3d} orbital and the TM_{3d}-O_{2p} hybridization. The suppressed hybridization results in the decreased intensity of the t_{2g} band that does not directly overlap with the O_{2p} orbital.[16]

2.3. Surface Structure of LMR-Nb

Surface doping enhances the electrochemical properties of the LMR-Nb between 2.0 and 4.8 V. The LMR-Nb exhibits a discharge capacity of 320 mAh g^{-1} at 0.1 C (1 C = 250 mA g^{-1}), in comparison with 276 mAh g^{-1} for the pristine LMR in the first cycle (**Figure 4**a). The capacity retention in the first 100 cycles increases from 76% for LMR to 95% for LMR-Nb. Moreover, the capacity of LMR-Nb is higher than that of LMR at any of the tested rates (Figure 4b). The increase of the capacity is attributed to the excess Li vacancies generated by the Nb^{5+} ions in the Li layer, which facilitates the fast Li diffusion therein. In addition, the initial coulombic efficiency increases from 81% for LMR to 87% for LMR-Nb, probably due to the inactivation of the surface oxygen as well as improved structural stability.

Dropping of the discharge potential of the LMR materials has been obsessing the materials scientists for decades though the discharge capacity has been stabilized to a great deal in recent years. Figure 4c shows that the discharge potential retention of LMR-Nb is remarkably enhanced; the discharge potential drops only 136 mV from the 6th to the 100th cycle. In contrast, the discharge potential of LMR declines by 593 mV in 100 cycles. In fact, most of the potential dropping for LMR-Nb occurs in the first 20 cycles while the potential decaying for LMR shows no trend of stopping till 100 cycles.

Figure S10 (Supporting Information) further shows that surface doping significantly improves the electrochemical performances at elevated temperature and enhances the thermal stability and safety of LMR-Nb as well. The heat generation is reduced from 107.18 J g^{-1} for LMR to 77.53 J g^{-1} for LMR-Nb (Figure 4d).

As discussed above, the strong ionic Nb—O bonding inactivates the surface oxygen and reduces the TM—O hybridization near the surface. As a result, the oxidation of the surface oxygen is suppressed or delayed to a higher potential. With the surface oxygen anchored, the TM migration that closely depends on the generation of oxygen vacancies becomes difficult. On the other hand, the strong Nb—O bonding inhibits the variation of the TM—O bond or the distortion of the TMO_6 octahedron, maintaining the integrity of the surface structure. In fact, the aforementioned inertness of the Mn^{4+} ions is also associated with the oxygen-anchoring effect of the doped Nb ions on the TMO_6 octahedron during cycling. These improvements are responsible for the enhanced electrochemical and thermal performances of LMR-Nb.

Similarly improved capacity and potential retention are obtained in Ti^{4+}- and Zr^{4+}-modified LMRs (Figure S11,

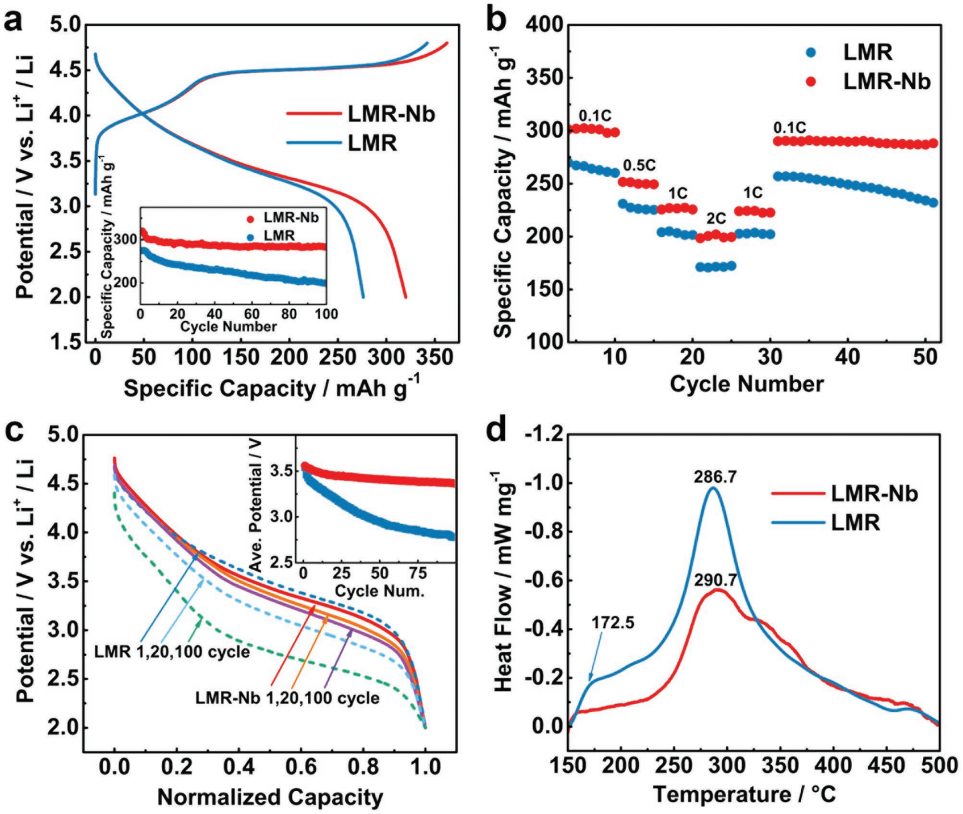

Figure 4. Comparison of the electrochemical (between 2.0 and 4.8 V) and thermal performances of LMR and LMR-Nb: a) initial charge/discharge profiles at a rate of 0.1 C (inset for the cycling performances); b) the rate performances; c) some selected normalized discharge potential profiles at 0.1 C (inset for the dependence of their average potentials on cycling number; solid lines for LMR-Nb and dash lines for LMR); d) DSC profiles of LMR and LMR-Nb changed to 4.8 V.

Supporting Information), illustrating the universality of our modification strategy on stabilizing the discharge potential and capacity but we will only focus on the discussion on LMR-Nb in this work.

2.4. Integrated Structure of LMR-Nb

The TM migration is known to start at the surface of a particle and propagate into the bulk of the Li-rich oxides.[6,21] Therefore, the robustness of the surface structure is critical in protecting the bulk structure from degradation while the integrity of the bulk structure guarantees the electrochemical and thermal stability of the material.

The protecting role of the Nb-doped surface layer remains effective after 20 or even 100 full charge/discharge cycles; surface doping drastically suppresses the propagation of the layered-to-spinel structural degradation. **Figure 5**a shows that the thickness of the surface layer of the LMR-Nb remains ≈5 atomic layers after the initial cycle. Heavy ions in the Li layer are found deeper under the surface (5–10 atomic layers) after 20 to 100 cycles (Figure 5b,c), but the difference between the bulk structures of the 20-cycled and the 100-cycled LMR-Nb samples is almost unrecognizable (Figure 5d,e). The line-scan intensity of the heavy ions in the Li layer in the bulk is only around 20% that of the TM ions in the TM layer in both the 20th and 100th cycled samples (Figure 5d,e). Cation mixing does not become more aggravated after 20 cycles though few TM ions can be detected in the Li layer, consistent with the suppressed potential dropping. Some TM ions appear in the Li layers occasionally after 100 cycles in LMR-Nb (Figure S12, Supporting Information), still distinct from that in LMR where a rocksalt-like phase forms on the surface and extends into the bulk.[21a] Obvious spinel phase is identified on the surface of LMR after the first cycle (Figure S13a, Supporting Information). After 20 cycles, the spinel phase transforms to a rocksalt-like phase and propagates a depth of ≈10 nm into the bulk (Figure S13b, Supporting Information).

The Raman spectroscopy is insensitive to the crystallinity of a material and can provide information on the general structure of a material, in comparison with the crystallinity-sensitive XRD technique or the local structure by STEM imaging. **Figure 6** compares the spectroscopic behavior of LMR and LMR-Nb upon repeated cycling. The weakening of the 490 and 605 cm^{-1} bands (for the E_g and A_{1g} modes of $LiNi_{1/3}Co_{1/3}Mn_{1/3}O_2$, respectively[22]) and the appearance of the band at ≈630 cm^{-1} (for the spinel-like phase and marked with red dash line in Figure 6a) suggest that the layered structure partially transforms into spinel after the initial cycling. The 630 cm^{-1} peak grows and becomes dominant after 50 cycles, evidencing the gradual layered-to-spinel transformation of LMR. However, no signals about the spinel phase are detected in the Raman

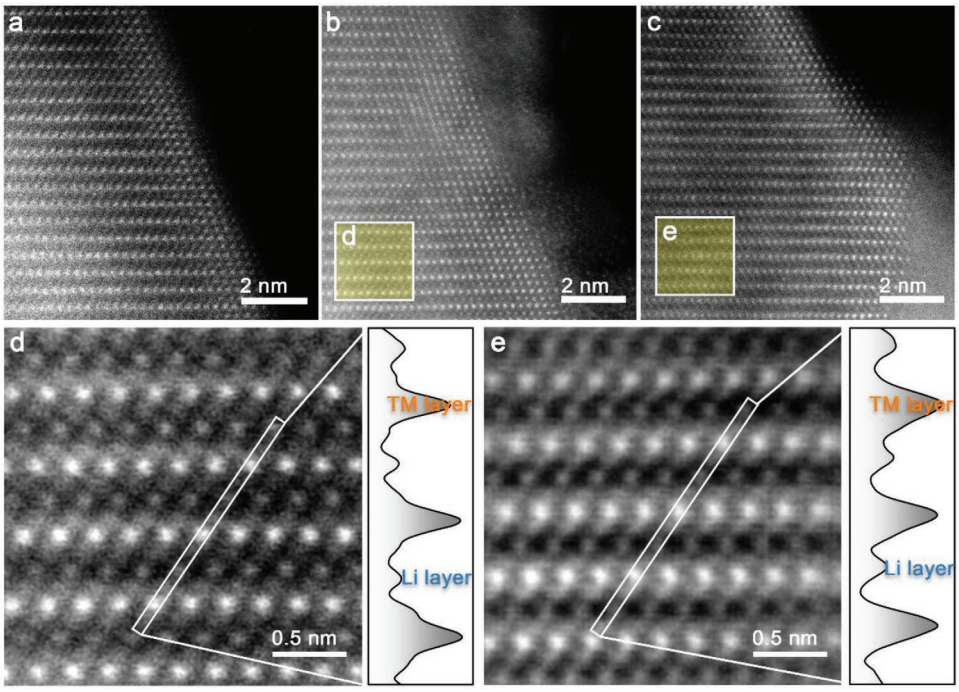

Figure 5. The HAADF images of the LMR-Nb a) after the initial cycle, b) after 20 cycles, and c) after 100 cycles between 2.0 and 4.8 V. (d) and (e) are the magnified images of the subsurface areas in (b) and (c), respectively.

spectrum of the 100-cycled LMR-Nb (Figure 6b), revealing that its layered structure is well maintained during cycling. These again prove the structural integrity of LMR-Nb.

3. Conclusions

In summary, surface doping was conducted to enhance the performances of $Li_{1.2}Mn_{0.54}Co_{0.13}Ni_{0.13}O_2$. The doped Nb^{5+} ions enter its Li layers by about five atomic layers and bind its O—TM(Li)—O slabs on and near the surface into an integrity. During charging, the oxygen in the bulk is oxidized but that near the surface remains inactive. The Mn^{4+} ions are fixed in the TM layer and kept inert during cycling, preventing the usual layered-to-spinel transformation and ensuring the structural stability. As a result, surface doping significantly suppresses the discharge potential dropping as well as boosts the initial coulombic efficiency, rate performance, and cycling and thermal stability of the material. Similar improvement was achieved in Ti and Zr surface-doped $Li_{1.2}Mn_{0.54}Co_{0.13}Ni_{0.13}O_2$ as well. Considering the universal effectiveness of the surface doping, our findings provide new insights into the fundamental understanding of structural degradation. It reveals that inactivating the surface oxygen and integrating the surface structure by strong metal-O bonding are critical for improving the structure and performance of the Li-rich layer-structured oxides. Investigation on the universality of the surface doping strategy on other layer-structured oxide cathode materials is in progress.

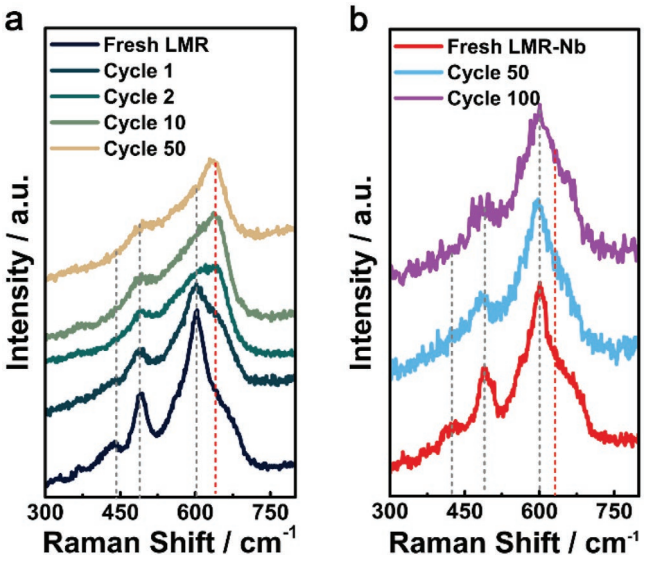

Figure 6. Raman spectra of a) LMR and b) LMR-Nb before and after various electrochemical cycles between 2.0 and 4.8 V.

4. Experimental Section

Material Preparation: The LMR was synthesized by a modified Pechini method. Stoichiometric amounts of $Co(CH_3COO)_2{\cdot}4H_2O$, $Ni(CH_3COO)_2{\cdot}4H_2O$, $Mn(CH_3COO)_2{\cdot}4H_2O$, and excess (5%) $LiCH_3COO{\cdot}H_2O$ were mixed and dissolved in deionized water together with citric acid and ethylene glycol (molar ratio = 1:4) to form a polymeric precursor. The LMR was obtained by at first heating the precursor at 400 °C for 5 h and then calcining it at 800 °C for 12 h in air.

As the first step toward surface doping, the fresh LMR powder was ground and dispersed in ethanol containing 3 at% niobium ethoxide. The suspension was ultrasonically processed and carefully dried before it was

annealed at 600 °C for 6 h in air. The Ti^{4+} and Zr^{4+} surface-doped LMRs were prepared similarly using titanium butoxide and zirconium nitrate. The actual Nb content in the final product (LMR-Nb) was determined by inductively coupled plasma-atomic emission spectroscopy (Shimadzu, ICPS-8100).

Cathode sheets were prepared by mixing the active material (LMR or LMR-Nb) with carbon black and polyvinylidene fluoride dissolved in *N*-methyl pyrrolidone at a weight ratio of 8:1:1 and then casting the slurry onto a piece of Al foil. The mass of the loaded active material was 2 to 3 mg cm^{-2} on the dried foil. Coin cells were assembled with fresh Li foil as the counter electrode, Celgard 2300 as the separator, and 1 mol L^{-1} $LiPF_6$ dissolved in a mixture of ethylene carbonate and dimethyl carbonate (EC:DMC = 1:1 v/v) as the electrolyte in an Ar-filled glove box.

Physical Characterization: The electrochemical cycling was performed on a LAND CT2001A battery tester in the galvanostatic mode between 2.0 and 4.8 V (vs Li^+/Li). The cells were disassembled in the glove box after galvanostatic cycling. The electrodes were rinsed with DMC and then vacuum-dried in the mini-chamber of the glove box before the subsequent characterizations.

The morphology of the material was characterized on a scanning electron microscope (Hitachi S-4800). The XRD patterns were collected between 10° and 80° (2θ) using the Cu Kα (λ = 1.5406 Å) radiation on a Bruker D8 Advance Diffractometer. The XRD patterns were refined by the Rietveld method using the TOPAS program. The aberration-corrected STEM observation was carried out on a JEOL ARM200F transmission electron microscope equipped with double C_S correctors for the condenser lens and objective lens. ABF and HAADF images were captured at acceptance angles of 11.5–23.0 and 90–370 mrad, respectively. High-resolution transmission electron microscopy characterization was performed using a JEOL 2010F transmission electron microscope operated at 200 keV at room temperature. The Raman spectra were recorded on a Renishaw Via-Reflex spectrometer (532 nm radiation) with a resolution of 2 cm^{-1}. The SXAS measurements through both TEY and FLY modes of Mn $L_{2,3}$ & O *K* edges and Nb L_3 edge were collected at the Spherical Grating Monochrometer beamline and Soft X-Ray Microcharacterization Beamline, respectively, at the Canadian Light Source, Saskatchewan, Canada. The X-ray absorption near edge spectroscopic analysis of the Co and Ni *K* edge was performed at the optical dispersive EXAFS beamline at the SOLEIL synchrotron, France. All the samples were transferred under proper protections in any of the above tests.

The method of the DFT calculations is described in detail in the Supporting Information.

Supporting Information

Supporting Information is available from the Wiley Online Library or from the author.

Acknowledgements

The authors appreciate Dr. Q. H. Li and X. Q. Yu in the Institute of Physics CAS, for their helpful discussion on the SXAS spectra. This work was financially supported by the National Key R&D Program of China (No. 2016YFB0100400), the National Key Development Program of China (No. 2015CB251100), and the National Natural Science Foundation of China (NSFC No. 51372268). The work at California State University Northridge was supported by the Army Research Office through the grant W911NF-15-1-0449.

Conflict of Interest

The authors declare no conflict of interest.

Keywords

lithium-rich materials, potential decay, surface doping

Received: July 9, 2018
Revised: August 20, 2018
Published online:

[1] M. M. Thackeray, C. S. Johnson, J. T. Vaughey, N. Li, S. A. Hackney, *J. Mater. Chem.* **2005**, *15*, 2257.
[2] J. M. Zheng, S. J. Myeong, W. R. Cho, P. F. Yan, J. Xiao, C. M. Wang, J. Cho, J. G. Zhang, *Adv. Energy Mater.* **2017**, *7*, 1601284.
[3] J. R. Croy, M. Balasubramanian, K. G. Gallagher, A. K. Burrell, *Acc. Chem. Res.* **2015**, *48*, 2813.
[4] X. Feng, Z. Yang, D. Tang, Q. Kong, L. Gu, Z. Wang, L. Chen, *Phys. Chem. Chem. Phys.* **2015**, *17*, 1257.
[5] a) P. K. Nayak, E. M. Erickson, F. Schipper, T. R. Penki, N. Munichandraiah, P. Adelhelm, H. Sclar, F. Amalraj, B. Markovsky, D. Aurbach, *Adv. Energy Mater.* **2018**, *8*, 1702397; b) X. Feng, Y. Gao, L. Ben, Z. Yang, Z. Wang, L. Chen, *J. Power Sources* **2016**, *317*, 74; c) S. H. Kang, K. Amine, *J. Power Sources* **2005**, *146*, 654.
[6] A. Boulineau, L. Simonin, J.-F. Colin, E. Canévet, L. Daniel, S. Patoux, *Chem. Mater.* **2012**, *24*, 3558.
[7] a) H. Koga, L. Croguennec, M. Ménétrier, P. Mannessiez, F. Weill, C. Delmas, *J. Power Sources* **2013**, *236*, 250; b) H. Koga, L. Croguennec, M. Menetrier, K. Douhil, S. Belin, L. Bourgeois, E. Suard, F. Weill, C. Delmas, *J. Electrochem. Soc.* **2013**, *160*, A786.
[8] a) C. R. Fell, D. Qian, K. J. Carroll, M. Chi, J. L. Jones, Y. S. Meng, *Chem. Mater.* **2013**, *25*, 1621; b) D. Qian, B. Xu, M. Chi, Y. S. Meng, *Phys. Chem. Chem. Phys.* **2014**, *16*, 14665.
[9] a) Y. R. Gao, X. F. Wang, J. Ma, Z. X. Wang, L. Q. Chen, *Chem. Mater.* **2015**, *27*, 3456; b) R. J. Xiao, H. Li, L. Q. Chen, *Chem. Mater.* **2012**, *24*, 4242; c) Y. Gao, J. Ma, Z. Wang, G. Lu, L. Chen, *Phys. Chem. Chem. Phys.* **2017**, *19*, 7025; d) M. Tian, Y. Gao, R. Xiao, Z. Wang, L. Chen, *Phys. Chem. Chem. Phys.* **2017**, *19*, 17538.
[10] a) Y. N. Zhou, J. Ma, E. Hu, X. Yu, L. Gu, K. W. Nam, L. Chen, Z. Wang, X. Q. Yang, *Nat. Commun.* **2014**, *5*, 5381; b) J. Ma, Y.-N. Zhou, Y. Gao, X. Yu, Q. Kong, L. Gu, Z. Wang, X.-Q. Yang, L. Chen, *Chem. Mater.* **2014**, *26*, 3256.
[11] J. Ma, Y.-N. Zhou, Y. Gao, Q. Kong, Z. Wang, X.-Q. Yang, L. Chen, *Chem. – Eur. J.* **2014**, *20*, 8723.
[12] S. D. Findlay, N. Shibata, H. Sawada, E. Okunishi, Y. Kondo, Y. Ikuhara, *Ultramicroscopy* **2010**, *110*, 903.
[13] a) A. Ito, Y. Sato, T. Sanada, M. Hatano, H. Horie, Y. Ohsawa, *J. Power Sources* **2011**, *196*, 6828; b) Y. Xu, E. Hu, F. Yang, J. Corbett, Z. Sun, Y. Lyu, X. Yu, Y. Liu, X.-Q. Yang, H. Li, *Nano Energy* **2016**, *28*, 164; c) M. Oishi, K. Yamanaka, I. Watanabe, K. Shimoda, T. Matsunaga, H. Arai, Y. Ukyo, Y. Uchimoto, Z. Ogumi, T. Ohta, *J. Mater. Chem. A* **2016**, *4*, 9293; d) W. E. Gent, K. Lim, Y. Liang, Q. Li, T. Barnes, S. J. Ahn, K. H. Stone, M. McIntire, J. Hong, J. H. Song, Y. Li, A. Mehta, S. Ermon, T. Tyliszczak, D. Kilcoyne, D. Vine, J. H. Park, S. K. Doo, M. F. Toney, W. Yang, D. Prendergast, W. C. Chueh, *Nat. Commun.* **2017**, *8*, 2091.
[14] F. Lin, Y. Liu, X. Yu, L. Cheng, A. Singer, O. G. Shpyrko, H. L. Xin, N. Tamura, C. Tian, T.-C. Weng, *Chem. Rev.* **2017**, *117*, 13123.
[15] W.-S. Yoon, M. Balasubramanian, K. Y. Chung, X.-Q. Yang, J. McBreen, C. P. Grey, D. A. Fischer, *J. Am. Chem. Soc.* **2005**, *127*, 17479.
[16] F. M. F. de Groot, M. Grioni, J. C. Fuggle, J. Ghijsen, G. A. Sawatzky, H. Petersen, *Phys. Rev. B* **1989**, *40*, 5715.

[17] N. Yabuuchi, M. Nakayama, M. Takeuchi, S. Komaba, Y. Hashimoto, T. Mukai, H. Shiiba, K. Sato, Y. Kobayashi, A. Nakao, M. Yonemura, K. Yamanaka, K. Mitsuhara, T. Ohta, *Nat. Commun.* **2016**, *7*, 13814.
[18] a) K. Luo, M. R. Roberts, R. Hao, N. Guerrini, D. M. Pickup, Y. S. Liu, K. Edstrom, J. Guo, A. V. Chadwick, L. C. Duda, P. G. Bruce, *Nat. Chem.* **2016**, *8*, 684; b) T. Mizokawa, Y. Wakisaka, T. Sudayama, C. Iwai, K. Miyoshi, J. Takeuchi, H. Wadati, D. G. Hawthorn, T. Z. Regier, G. A. Sawatzky, *Phys. Rev. Lett.* **2013**, *111*, 056404.
[19] G. Assat, J.-M. Tarascon, *Nat. Energy* **2018**, *3*, 373.
[20] F. M. F. de Groot, *J. Electron Spectrosc. Relat. Phenom.* **1994**, *67*, 529.
[21] a) J. Zheng, P. Xu, M. Gu, J. Xiao, N. D. Browning, P. Yan, C. Wang, J.-G. Zhang, *Chem. Mater.* **2015**, *27*, 1381; b) K. Jarvis, C.-C. Wang, M. Varela, R. R. Unocic, A. Manthiram, P. J. Ferreira, *Chem. Mater.* **2017**, *29*, 7668.
[22] C. Venkateswara Rao, J. Soler, R. Katiyar, J. Shojan, W. C. West, R. S. Katiyar, *J. Phys. Chem. C* **2014**, *118*, 14133.